Accounting for Optical Generation in the Quasi-Neutral Regions of Perovskite Solar Cells

Parnian Ferdowsi, Farzan Jazaeri, Efrain Ochoa-Martinez, Jovana Milic, Michael Saliba, Ullrich Steiner, and Jean-Michel Sallese

***Abstract*— Predicting the performance of solar cells though analytical models is important for the theory-guided optimisation of these devices. Earlier models neglect the impact of the optical generation in the quasi-neutral regions of a perovskite solar cell. Here, a new model is developed that takes optical generation in these regions into account. The model includes the full depletion approximation and the drift-diffusion transport mechanisms. A comparison with earlier models demonstrates the improved predictive power of the developed model. In addition, the accuracy of the model was assessed by comparing it prediction to experimental data obtained from working devices.**

***Index Terms*— perovskite solar cells, physical modeling, optical generation, quasi-neutral regions.**

I. Introduction

ORGANIC–inorganic lead halide perovskite solar cells (PSCs) are considered to be among the most promising photovoltaic technologies that have generated intense research in the past decade after they demonstrated outstanding light-harvesting characteristic, high power-conversion efficiency (PCE), low cost, and ease of fabrication [1], [2]. Since 2009, the power conversion efficiency of PSCs has been improved dramatically starting from 3.8% [3] to the current world record of 25.2% [4]. This was possible due to many improvements in terms of solvents, interfaces, and materials optimizations. The perovskite materials used in photovoltaics have the ABX_3 composition consisting of of an organic/inorganic monovalent cation, A [Cs^+], methylammonium [MA^+], or formamidinium [FA^+]; a divalent metal, B (Pb^{2+}); and a halide anion, X (Cl^-, Br^- or I^-) [2]. There is an ongoing need to better understand the fundamental processes and mechanisms underlying their photovoltaic behavior.

Modeling is a necessary step towards the development and manufacturing of these solar cells. The experimental efforts can be supported by modeling and simulations [5]–[8]. Modeling of photovoltaic cells has been carried out over a period of 40 years [9]–[11], when some simplified analytical expressions were proposed for the output characteristics ($I-V$) in PVs, with assumptions that are still widely accepted and implemented in present models of PSCs. The current-voltage characteristic of a photovoltaic cell informs about its solar energy conversion ability and efficiency. To the best of our knowledge, all previously developed models neglect the impact of optical generation of minority carriers in the quasi-neutral regions of PSCs, an assumption which has not been justified [6], [12]–[15].

Parnian Ferdowsi (E-mail: Parnian.Ferdowsi@unifr.ch), Efrain Ochoa-Martinez, Jovana Milic, and Ullrich Steiner are with Adolphe Merkle Institute, University of Fribourg, CH 1700, Fribourg, Switzerland. Farzan Jazaeri and Jean-Michel Sallese are with Electron Device Modeling and Technology Laboratory (ED-LAB), Ecole Polytechnique Fédérale de Lausanne,1015 Lausanne, Switzerland. Michael Saliba is with Institute for Photovoltaics (IPV), University of Stuttgart, Pfaffenwaldring 47, 70569 Stuttgart, Germany.

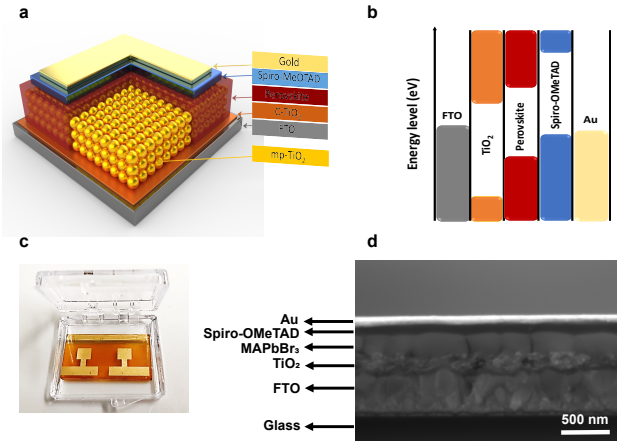

Fig. 1. (a) Schematic of a standard perovskite solar cell structure, (b) Energy level diagram, (c) Fabricated $MAPbBr_3$ device, (d) SEM cross-section of a PSC. (FTO: Fluorine doped tin oxide, Spiro-OMeTAD:2,2',7,7'-Tetrakis[N,N-di(4-methoxyphenyl)amino]-9,9' spirobifluorene)

Here, we demonstrate that such a simplification does not correctly predict the output characteristics of PSCs. The simplified models can fit the experimental data, but at the expense of introducing non-physical fitting parameters, i.e. they fail in predicting the device characteristics as experimental parameters are changed.

While the assumption of optical generation is often included in commercial and self-written numerical simulators, they are not based on fundamental physical principles at both the theoretical and the experimental levels.

The basic idea of this study is to develop a new analytical and physics-based model of perovskite photovoltaic cells that can predict the device characteristics from the device parameters, which is different to existing models, enabling us to address the underlying physics that was not correctly described in the earlier models.

Relying on the drift-diffusion transportation mechanism, this work derives a model for the output characteristic of PSCs that includes the optical generation of minority carriers in the quasi-neutral regions. The model is validated against the experimental data of fabricated perovskite-based solar cells. Finally, we demonstrate how this new model can be used to obtain physical parameters of a PSC and how its efficiency can be improved.

II. Device Structure and Operation Principle

In the perovskite-based solar cell structure, the undoped perovskite layer is sandwiched between electron (ETL) and

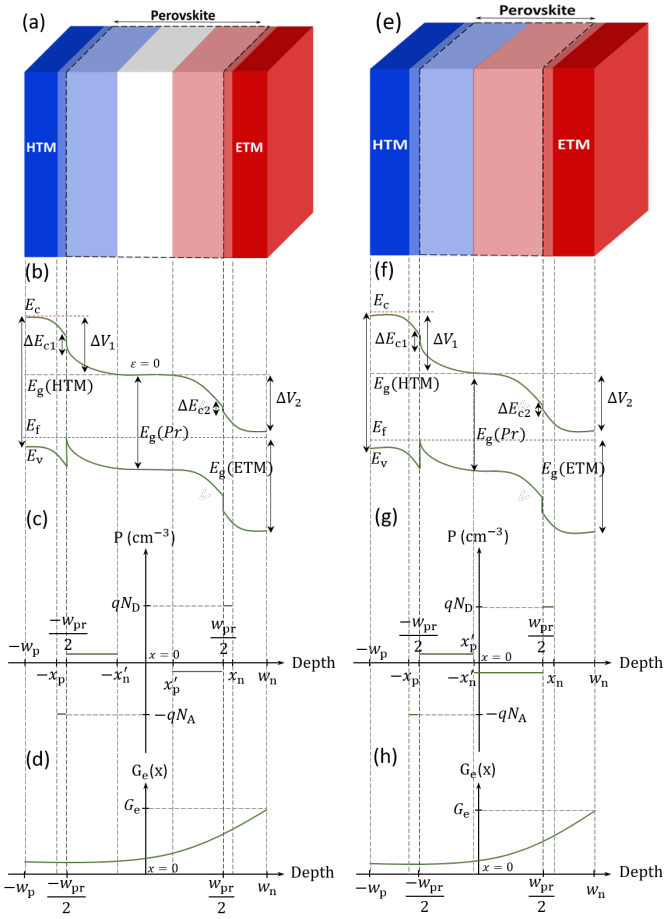

Fig. 2. Schematics of typical PSC device structures, energy level diagrams, doping concentrations, and optical generation profiles of partially depleted (a, b, c, d) and fully depleted (e, f, g, h) provskite layers in PSCs. The depletion regions are identified by light blue and red colors in (a) and (e) while quasi neutral regions are coloured in dark blue and red. The neutral region in the center of perovskite layer remains white.

hole (HTL) transport layers made from, i.e., TiO_2 and Spiro-OMeTAD, respectively, with both semiconductor material having a wider band gap than the perovskite (Fig. 1). This can be represented by a simplified n-i-p architecture (Fig. 2), consisting of two heterojunctions in series with two built-in potentials, V_{bi1} and V_{bi2}, one between the HTL and perovskite and the second is between the TiO_2 and the perovskite. Holes are the majority carriers in HTL layer and they diffuse towards the perovskite film where electron and hole concentrations give rise to the intrinsic carrier density. Conversely, electrons diffuse towards the HTL layer. Electrons are the majority carriers in the ETL and they diffuse to the perovskite semiconductor and holes diffuse towards the ETL. If the perovskite layer is doped and/or sufficiently thick (Fig. 2a,b), neutral zone forms in the centre of the perovskite layer, where the electrostatic potential is almost constant and the electric field vanishes. Therefore, drift currents are limited to optically generated carriers within the very thin depletion regions next to the junctions. However, the doping concentration in the perovskite layer is typically much lower compared to the transport layers, so that *full depletion* can be assumed (Fig. 2e,f). This implies that the two depleted regions of two heterojunctions intersect at one point and free carrier concentrations are negligible compared to the fixed charge density in the perovskite film.

III. Modeling of Perovskite-based Solar Cells

Perovskite-based solar cell as depicted in Fig. 2e were modeled. The core model assumes an ideal solar cell, ignoring interface charge traps. When calculating the diffusion current in a solar cell the minority carrier concentrations in the *n*-type and *p*-type quasi-neutral regions (the ETL and HTL) need to be known, in the presence of optical generation. In previous studies, the generation term in the quasi-neutral regions was assumed to be zero and therefore the diffusion current was simply the dark current, a simplification that cannot be justified [6], [12]–[15]. To the best of our knowledge, this assumption is still widely accepted and implemented in present models of PSC. While such a simple approach can fit the experimental data, it fails at predicting the device characteristics if any of the device parameters is changed. In our analysis, the minority carrier profiles are obtained by applying the boundary conditions at the edges of the depletion regions in the ETL and HTL. An important point is that these profiles are a function of the voltage across the entire solar cell, V_{L}, which is also linked to the drift current and incident photon flux.

We derive a general expression to obtain the minority-carrier densities in the ETL and HTL layers, while taking the optical generation of the minority carriers in the *n*-type and *p*-type quasi-neutral regions into account. Then, neglecting the influence of the optical generation on the minority carriers, we discuss the validity of this widely accepted assumption and prove that leads to inconsistent predictions.

A. General Approach

To simplify the analysis, an abrupt transition between the neutral and depleted region is used to solve in one-dimensional (1-D) Poisson equation with a full depletion approximation. We consider the heterojunction as a homojunction with smooth transitions of ΔE_{c} and ΔE_{v} inside the depletion region, which has been widely used in the earlier approaches [16]. With this assumption, the analysis can be greatly simplified and, the diffusion currents are similar to regular *p-n* junctions with the appropriate parameters in place. Therefore, the band offsets ΔE_{c} and ΔE_{v} and derivative discontinuities do not exist at our generation rates. Each diffusion current component depends on the properties of the diffusion side only, as is the case in a homojunction. This assumption has been already proposed and is well explained in [16].

In addition, we took the impact of the discontinuity at the conduction- and valence-band edges on the electrostatics into account by solving the Poisson equation for a step junction while introducing the built-in potentials as parameters.

It is worth mentioning that a precise estimation of the voltage-dependent charge collection at the heterojunction has been always a challenge in PSCs. This might affect cell efficiency and carrier transport (*J-V* and *C-V*) under light and dark conditions [17], [18]. This is however not taken into account in the core model, which intends to capture the essential physics in this type of solar cells.

In equilibrium, the majority carrier density in the HTL at the edge of the depletion region ($x = -x_{\mathrm{p}}$) is obtained

TABLE I
LIST OF SYMBOLS USED IN THE MODEL DERIVATIONS IN THIS STUDY.

Description	Symbol	Unit
Built-in potentials	$V_{\rm bi1}$ $V_{\rm bi2}$	V
Electron charge	q	C
Thermal voltage	$U_{\rm T}$	V
Potential profile	ψ	V
Bottom of the conduction band	$E_{\rm C}$	eV
Top of the valence band	$E_{\rm V}$	eV
Fermi level	$E_{\rm F}$	eV
Electric field	$\mathscr{E}$	V/m
Density of hole transport Layer	$N_{\rm A}$	$\rm cm^{-3}$
Density of electron transport Layer	$N_{\rm D}$	$\rm cm^{-3}$
Thickness of perovskite layer	$W_{\rm pr}$	m
Majority carrier densities	$p_{\rm p}, n_{\rm n}$	$\rm cm^{-3}$
Minority carrier densities	$n_{\rm p}, p_{\rm n}$	$\rm cm^{-3}$
Output voltage	$V_{\rm L}$	V
Conduction band discontinuities	$\Delta E_{\rm c1}$ $\Delta E_{\rm c2}$	eV
e/h excess carrier concentration	Δn, Δp	$\rm cm^{-3}$
e/h coefficient	$D_{\rm n}$, $D_{\rm p}$	$\rm cm^2/s$
e/h diffusion length	$L_{\rm n}$, $L_{\rm p}$	m
e/h mobility	$\mu_{\rm n}$, $\mu_{\rm p}$	$\rm cm^2/V\,s$

as $p_{\rm p}(-x_{\rm p}) = p_{\rm n^-} \exp(V_{\rm bi1}/U_{\rm T})$, where $p_{\rm n^-}$ is the hole carrier density in the perovskite film, which is linked to the minority carrier density in the TiO_2 layer, $p_{\rm n0}$, through $p_{\rm n^-} = p_{\rm n0} \exp(V_{\rm bi2}/U_{\rm T})$, yielding

$$p_{\rm p}(-x_{\rm p}) = p_{\rm n0} \exp\left(\frac{V_{\rm bi1}+V_{\rm bi2}}{U_{\rm T}}\right). \tag{1}$$

Similarly, in equilibrium, the majority carrier density in the ETL at the edge of the depletion region ($x = x_{\rm n}$) is given by

$$n_{\rm n}(x_{\rm n}) = n_{\rm p0} \exp\left(\frac{V_{\rm bi1}+V_{\rm bi2}}{U_{\rm T}}\right). \tag{2}$$

Since solar cells operate under a forward bias, $V_{\rm L}$, equations (1) and (2) are rewritten for non-equilibrium conditions, i.e. $V_{\rm L} \neq 0$,

$$p_{\rm p}(-x_{\rm p}) = p_{\rm n}(x_{\rm n}) \exp\left(\frac{V_{\rm bi1}+V_{\rm bi2}-V_{\rm L}}{U_{\rm T}}\right), \tag{3}$$

$$n_{\rm n}(x_{\rm n}) = n_{\rm p}(-x_{\rm p}) \exp\left(\frac{V_{\rm bi1}+V_{\rm bi2}-V_{\rm L}}{U_{\rm T}}\right), \tag{4}$$

where $p_{\rm n}(x_{\rm n})$ and $n_{\rm p}(-x_{\rm p})$ are the minority carrier densities, including the excess carrier concentrations at the edge of the depletion region, given by $p_{\rm n}(x_{\rm n}) = p_{\rm n0} + \Delta p$ and $n_{\rm p}(-x_{\rm p}) = n_{\rm p0} + \Delta n$ with Δn and Δp the excess electron and hole carrier concentrations. Both, $p_{\rm n}(x_{\rm n})$ and $n_{\rm p}(-x_{\rm p})$ depend on $V_{\rm L}$ through the exponential terms.

Dividing (1) by (3) and (2) by (4) leads to a set of boundary conditions for the minority carriers in non-equilibrium, at the edges of the depletion regions of ETL and HTL layers,

$$\begin{aligned} p_{\rm n}(x_{\rm n}) &= p_{\rm n0} \exp\left(\frac{V_{\rm L}}{U_{\rm T}}\right) \text{ and} \\ n_{\rm p}(-x_{\rm p}) &= n_{\rm p0} \exp\left(\frac{V_{\rm L}}{U_{\rm T}}\right). \end{aligned} \tag{5}$$

In addition, the carrier density at the metal contacts is assumed to equal the thermal-equilibrium carrier density without excess carriers since these will recombine at the contact, resulting in a further set of boundary conditions

$$n_{\rm p}(-w_{\rm p}) = n_{\rm p0} \quad \text{and} \quad p_{\rm n}(w_{\rm n}) = p_{\rm n0}. \tag{6}$$

Next, the minority-carrier densities in the ETL and HTL are determined from the 1D diffusion-continuity equations,

$$D_{\rm p}\frac{\partial^2 p_{\rm n}}{\partial x^2} - \frac{p_{\rm n}-p_{\rm n0}}{\tau_{\rm p}} + G_{\rm e}(x) = 0, \tag{7}$$

$$D_{\rm n}\frac{\partial^2 n_{\rm p}}{\partial x^2} - \frac{n_{\rm p}-n_{\rm p0}}{\tau_{\rm n}} + G_{\rm e}(x) = 0, \tag{8}$$

where $D_{\rm n} = \mu_{\rm n} U_{\rm T}$, and $D_{\rm p} = \mu_{\rm p} U_{\rm T}$ are the carrier diffusion constants, $\mu_{\rm n}$ and $\mu_{\rm p}$ are electron and hole carrier mobilities, $\tau_{\rm n}$ and $\tau_{\rm p}$ are the lifetimes of excess carriers, and $p_{\rm n0}$ and $n_{\rm p0}$ the equilibrium hole and electron densities.

Both thermal carrier generation and recombination losses for electrons and holes have been taken into account in the 1D diffusion-continuity equations, i.e. (7) and (8), where the total steady-state generation and recombination rates of carriers per unit volume are given by $(p_{\rm n}-p_{\rm n0})/\tau_{\rm p}$ and $(n_{\rm p}-n_{\rm p0})/\tau_{\rm n}$, with $\tau_{\rm n}$ and $\tau_{\rm p}$ the "average" lifetime for electrons and holes). Indeed, combining (7) and (8), while including the terms of carrier recombination leads to the Shockley-Read-Hall expression for the trap-assisted recombination.

The term $G_{\rm e}(x)$ is the electron-hole generation rate is given by

$$G_{\rm e}(x) = \phi_0 \alpha \exp\left[\alpha\,(x-w_{\rm n})\right], \tag{9}$$

where ϕ_0 is the incident photon flux per unit area given by $P_{\rm opt}(1-R)/Ah\nu$, R is the reflection coefficient, A is the device area, α is the absorption coefficient, $P_{\rm opt}$ is the incident optical power, and $h\nu$ is the photon energy.

The fact that the impact of refractive index has been taken into account through (9) where the reflection coefficient, i.e. R, determines the flux which enters into the solar cell through the incident optical power, which gives the electron-hole generation rate within the solar cell.

It is worth mentioning that relation (9) is not limited to thick silicon solar cells. It represents an energy dependent absorption profile, where α depends on the photon energy. Nevertheless, the validity of the core model is verified throughout this article by comparing it with an ideal device for a given wavelength to ensure that it captures the essential physicsof the solar cells. In case of many wavelengths, (9) has to be integrated over energy. That becomes necessary because the quasi-neutral regions (ETL and HTL) have band-gaps of ca. $3-3.2$ eV [19], i.e., they absorb in the spectral range of ca. $385-415$ nm. By integrating over this wavelength. range, (9) remains valid and the energy-dependent absorption profile does not need to be taken into account in the core model. The number of photons

TABLE II

PREVIOUSLY DEVELOPED MODELS FOR THICK (1) AND THIN (2) TRANSPORTATION LAYERS AND OUR APPROACH (3) THAT INCLUDES OPTICAL GENERATION IN THE DIFFUSION CURRENT.

N.	Models	Description	Diffusion Models
1	Simplified Model (29)	Dark current T_e & $T_h \gg L_n$ & L_p	$I_{diff} = qA\left(\frac{D_n n_{p0}}{L_n} + \frac{D_p p_{n0}}{L_p}\right)\left[\exp\left(\frac{V_L}{U_T}\right) - 1\right]$
2	Simplified Model (26)	Dark current for all thicknesses of ETL & HTL	$I_{diff} = I_s\left[\exp(V_L/U_T) - 1\right]$
			$I_s = qA\left[\frac{D_n n_{p0}}{L_n}\coth\left(\frac{w_p - x_p}{L_n}\right) + \frac{D_p p_{n0}}{L_p}\coth\left(\frac{w_n - x_n}{L_p}\right)\right]$
3	Present Model	Dark Current	$J_{p,diff}\,\vert_{x=x_n} = -qD_p\left\{\frac{c_1}{L_p} - \frac{c_2}{L_p} + k_p\alpha\exp\left[\alpha\left(x_n - w_n\right)\right]\right\}$
		+	$J_{n,diff}\,\vert_{x=-x_p} = qD_n\left\{\frac{c_1'}{L_n} - \frac{c_2'}{L_n} + k_n\alpha\exp\left[-\alpha\left(x_p + w_p\right)\right]\right\}$
		Optical Generation in thin ETL & HTL	$I_{diff} = A(J_{n,diff} + J_{p,diff})$

arriving per second per area is given by ϕ_0 (power/photon energy) in the spectral distribution of illumination.

Therefore, considering a beam of light, used in our experiments (Section IV), with a power of 100m Watt/cm^2 and a wavelength of 385 nm leads to $\phi_0 = 1.9 \times 10^{21}$ photons/m^{2}s.

The general solution of (7) and (8), before applying the boundary conditions, are thus given by

$$p_n = C_1 \exp\left(\frac{x - x_n}{L_p}\right) + C_2 \exp\left(-\frac{x - x_n}{L_p}\right) + p_{n0} + k_p \exp\left[\alpha\left(x - w_n\right)\right], \tag{10}$$

$$n_p = C_1' \exp\left(\frac{x + x_p}{L_n}\right) + C_2' \exp\left(-\frac{x_p + x}{L_n}\right) + n_{p0} + k_n \exp[\alpha(x - w_n)], \tag{11}$$

where $L_n = \sqrt{D_n\tau_n}$ and $L_p = \sqrt{D_p\tau_p}$ are the diffusion lengths for electrons and holes and k_n and k_p are given by

$$k_p = \frac{\tau_p\phi_0\alpha}{1 - \tau_p D_p\alpha^2} \quad \text{and} \quad k_n = \frac{\tau_n\phi_0\alpha}{1 - \tau_n D_n\alpha^2}. \tag{12}$$

Applying the boundary conditions (5) and (6) to (10) and (11) yields

$$C_1 = \frac{[p_{n0}(1 - e^{V_L/U_T}) + k_p e^{-\alpha T_e}]e^{-T_e/L_p} - k_p}{2\sinh\left(T_e/L_p\right)}, \tag{13}$$

$$C_2 = p_{n0}(e^{V_L/U_T} - 1) - k_p e^{-\alpha T_e} - C_1, \tag{14}$$

$$C_1' = \frac{[n_{p0}(1 - e^{V_L/U_T}) + k_n e^{-\alpha T_{pe}}]e^{T_h/L_n} - k_n e^{-\alpha T}}{2\sinh\left(-T_h/L_n\right)}, \tag{15}$$

$$C_2' = n_{p0}(e^{V_L/U_T} - 1) - k_n e^{-\alpha T_{pe}} - C_1', \tag{16}$$

where thicknesses of the layers are given by $T_e = w_n - x_n \approx T_{TiO_2}$, $T_{pe} = w_n + x_p \approx T_{TiO_2} + W_{pr}$, $T_h = w_p - x_p \approx T_{Spiro}$ and $T = w_n + w_p \approx T_{TiO_2} + W_{pr} + T_{Spiro}$.

Under steady-state conditions the total photocurrent density is given by

$$J_{tot} = J_{drif} + J_{diff}, \tag{17}$$

where $J_{diff} = J_{n,diff} + J_{p,diff}$ corresponds to the flow of carriers from higher to lower concentrations, as determined by the 1D diffusion equation. Obtaining the excess carrier distributions from (10) and (11), the total diffusion current density due to carriers generated outside of the depletion layer is given by

$$J_{p,diff}\,\vert_{x=x_n} = -qD_P\frac{\mathrm{d}p_n(x)}{\mathrm{d}x}\,\vert_{x=x_n} = -qD_p\left\{\frac{c_1}{L_p} - \frac{c_2}{L_p} + k_p\alpha\exp\left[\alpha\left(x_n - w_n\right)\right]\right\}, \tag{18}$$

$$J_{n,diff}\,\vert_{x=-x_p} = qD_n\frac{\mathrm{d}n_p(x)}{\mathrm{d}x}\,\vert_{x=-x_p} = qD_n\left\{\frac{c_1'}{L_n} - \frac{c_2'}{L_n} + k_n\alpha\exp\left[-\alpha\left(x_p + w_p\right)\right]\right\}. \tag{19}$$

The drift current $J_{drift} = J_{n,drift} + J_{p,drift}$ arises from free carriers generated within the depletion region, i.e. within the perovskite film. Assuming a graded junction where ΔE_c and ΔE_v are smooth transitions inside the depletion region, the analysis can be simplified. The drift current is then given by

$$J_{drift} = -q\int_{-W_{pr}/2}^{W_{pr}/2} G_e(x)\mathrm{d}x = J_0\sinh\left(\frac{\alpha W_{pr}}{2}\right), \tag{20}$$

where $J_0 = 2q\phi_0\exp(\alpha w_n)$. Note that carrier recombination is neglected within the absorption layer due to the long diffusion lengths in the perovskite. Note also that the proposed model takes the electrostatic distortion into account, which is caused by the screening of the electric field by 'ions' within the perovskite layer through relations (1) - (4). The distribution of ions is assumed to arise from ionized dopant impurities that are uniform within each layer. Their contribution is incorporated through the built-in potentials, V_{bi1} and V_{bi2} in relations (1) - (4). The electrostatic impact of these ions is translated into the band structure distortion by modifying the built-in potentials through the solution of the Poisson equation (i.e. leading to a parabolic solution of Poisson's equation when these distributions are uniform) between the HTL and ETL and perovskite film. This indirectly affects the minority carrier densities p_{n0} and n_{p0} and therefore the saturation current. Therefore, adding additional ions which are not coming from ionized dopants will not change the analysis. These ions simply impact the diode parameters such as the saturation current and the built-in potentials, V_{bi1} and V_{bi2} , but not the $I-V$ characteristics. When extracting the model parameters from measurements, these considerations are taken into account.

TABLE III
PARAMETERS OF THE STUDIED SOLAR CELL.

Parameter	Symbol	Value
Perovskite band gap	E_{g}	1.55eV [20]
ETL band gap	$E_{\mathrm{g}}(ETL)$	3.0eV [19]
HTL band gap	$E_{\mathrm{g}}(HTL)$	3.2eV [19]
Effective VB DoS of perovskite	$N_{\mathrm{V,Pr}}$	$10^{17}\mathrm{cm}^{-3}$ [21]
Effective CB DoS of perovskite	$N_{\mathrm{C,Pr}}$	$10^{19}\ \mathrm{cm}^{-3}$ [21]
Perovskite intrinsic density	n_{i}	$9\times10^{4}\,\mathrm{cm}^{-3}$
Thickness of perovskite layer	W_{pr}	450 nm
Doping of HTL	N_{A}	$10^{16}\,\mathrm{cm}^{-3}$
Doping of ETL	N_{D}	$5.06\times10^{16}\,\mathrm{cm}^{-3}$
Electron mobility of ETL	μ_{n}	$10.0\,\mathrm{cm}^2/\mathrm{V\,s}$
Hole mobility of HTL	μ_{p}	$3.1\mathrm{cm}^2/\mathrm{V\,s}$
Electron life time in ETL	τ_{n}	10^{-6} s
Hole life time in HTL	τ_{p}	10^{-6} s
Electron diffusion coefficient	D_{n}	$0.271\,\mathrm{cm}^2/\mathrm{s}$
Hole diffusion coefficient	D_{p}	$0.08127\,\mathrm{cm}^2/\mathrm{s}$
Electron diffusion length	L_{n}	$5.2\times10^{-6}\mathrm{m}$
Hole diffusion length	L_{p}	$2.85\times10^{-6}\mathrm{m}$

DoS: Density of state

B. Simplified Analytical Approach

Neglecting optical generation on the minority carrier profile in the quasi neutral TiO_2 and Spiro films in (7) and (8) and applying the boundary conditions (5) and (6) leads to the following minority carrier densities in the quasi-neutral regions,

$$p_{\mathrm{n}}=p_{\mathrm{n0}}+\eta\left[\cosh\frac{x-x_{\mathrm{n}}}{L_{\mathrm{p}}}-\coth\frac{w_{\mathrm{n}}-x_{\mathrm{n}}}{L_{\mathrm{p}}}\sinh\frac{x-x_{\mathrm{n}}}{L_{\mathrm{p}}}\right] \quad (21)$$

$$n_{\mathrm{p}}=n_{\mathrm{p0}}+\theta\left[\cosh\frac{x-x_{\mathrm{p}}}{L_{\mathrm{n}}}-\coth\frac{w_{\mathrm{p}}-x_{\mathrm{p}}}{L_{\mathrm{n}}}\sinh\frac{x+x_{\mathrm{p}}}{L_{\mathrm{n}}}\right] \quad (22)$$

where $\eta/p_{\mathrm{n0}}=\theta/n_{\mathrm{p0}}=[\exp(V_{\mathrm{L}}/U_{\mathrm{T}})-1]$. The current density in each quasi-neutral region is obtained by calculating the diffusion current density using equations (18) and (19),

$$J_{\mathrm{p,diff}}\,|_{x=x_{\mathrm{n}}}=-qD_{\mathrm{P}}\frac{\mathrm{d}p_{\mathrm{n}}(x)}{\mathrm{d}x}\,|_{x=x_{\mathrm{n}}}=\frac{qD_{\mathrm{P}}\eta}{L_{\mathrm{p}}}\coth\left(\frac{w_{\mathrm{n}}-x_{\mathrm{n}}}{L_{\mathrm{p}}}\right), \quad (23)$$

$$J_{\mathrm{n,diff}}\,|_{x=-x_{\mathrm{p}}}=qD_{\mathrm{n}}\frac{\mathrm{d}n_{\mathrm{p}}(x)}{\mathrm{d}x}\,|_{x=-x_{\mathrm{p}}}=\frac{qD_{\mathrm{n}}\theta}{L_{\mathrm{n}}}\coth\left(\frac{w_{\mathrm{n}}-x_{\mathrm{p}}}{L_{\mathrm{n}}}\right). \quad (24)$$

The total diffusion current is then given by

$$I_{\mathrm{diff}}=A(J_{\mathrm{n,diff}}+J_{\mathrm{p,diff}})=I_{\mathrm{s}}\left[\exp(V_{\mathrm{L}}/U_{\mathrm{T}})-1\right], \quad (25)$$

where I_{s} can be written as

$$\frac{I_{\mathrm{s}}}{qA}=\left[\frac{D_{\mathrm{n}}n_{\mathrm{p0}}}{L_{\mathrm{n}}}\coth\left(\frac{w_{\mathrm{p}}-x_{\mathrm{p}}}{L_{\mathrm{n}}}\right)+\frac{D_{\mathrm{p}}p_{\mathrm{n0}}}{L_{\mathrm{p}}}\coth\left(\frac{w_{\mathrm{n}}-x_{\mathrm{n}}}{L_{\mathrm{p}}}\right)\right] \quad (26)$$

and A is the area of the solar cell. Note that the total drift current is still given by (20).

In addition, in case $\phi_0=0$, i.e. optical generation does not take place in the quasi-neutral regions and thus $k_{\mathrm{p}}=k_{\mathrm{n}}=0$, cancelling the RHS terms in (18) and (19). In this special case, both the simplified and general approaches lead to the same results.

When the thicknesses of the quasi neutral regions become larger than the minority-carrier diffusion lengths, (21) and (22) can be simplified to

$$p_{\mathrm{n}}=p_{\mathrm{n0}}+\eta\exp\left(-\frac{x-x_{\mathrm{n}}}{L_{\mathrm{p}}}\right), \quad (27)$$

$$n_{\mathrm{p}}=n_{\mathrm{p0}}+\theta\exp\left(-\frac{x+x_{\mathrm{p}}}{L_{\mathrm{n}}}\right). \quad (28)$$

Then, the total diffusion current is simplified to

$$I_{\mathrm{diff}}=qA\left(\frac{D_{\mathrm{n}}n_{\mathrm{p0}}}{L_{\mathrm{n}}}+\frac{D_{\mathrm{p}}p_{\mathrm{n0}}}{L_{\mathrm{p}}}\right)\left[\exp\left(\frac{V_{\mathrm{L}}}{U_{\mathrm{T}}}\right)-1\right]. \quad (29)$$

Even though (29) is widely used and generally accepted to study the impact of physical parameters on the output characteristics of photovoltaic cells, it fails at predicting accurately the influence of the parameters on the photovoltaic cells with thin quasi neutral regions. In addition, this oversimplified model underestimates the contribution of the diffusion terms related to the optical generation in the quasi neutral regions. It is worth mentioning that this will have no impact on the total current and other PSC parameters if the ETL and HTL are transparent. The proposed approach and previously developed models are summarized in Table II and they were implemented to extract the PV cell parameters from the experimental $I-V$ characteristics of our devices.

C. Model comparisons and improvement

To better understand the impact of the optical generation on minority carriers in the *n*-type and *p*-type quasi-neutral regions, we compare the $I-V$ output characteristics obtained from the simplified model where the optical generation is ignored in the quasi-neutral regions, and the proposed model in the presence of optical generation.

Fig. 3 shows the diffusion current-voltage characteristics predicted by the three models of a photovoltaic with the parameters listed in Table III. Fig 3a compares the diffusion current calculated with the simplified models given by (25) and (29) for a device with thick ETL and HTL ($T_{\mathrm{e}}=T_{\mathrm{h}}=10\,\mu\mathrm{m}$). In this case, the thicknesses of the quasi-neutral regions are larger than the minority-carrier diffusion lengths and no dependence of transport layer thicknesses are expected and both simplified models accurately predict the dark current.

However, as soon as the transport layer thicknesses are reduced to values below the minority-carrier diffusion lengths ($T_{\mathrm{e}}=T_{\mathrm{h}}=200\,\mathrm{nm}$), the simplified model of (29) fails in predicting the dark current of the device, with a large mismatch in the open-circuit voltage predicted by the two simplified models (Fig 3b).

Fig 3c compares the $I-V$ characteristics obtained from our model (18),(19), and (20), with the two simplified models in the dark, for a device with thin transport layers ($T_{\mathrm{e}}=T_{\mathrm{h}}=150\,\mathrm{nm}$). Again, the widely used simplified model of (29) fails at correctly predicting the dark current.

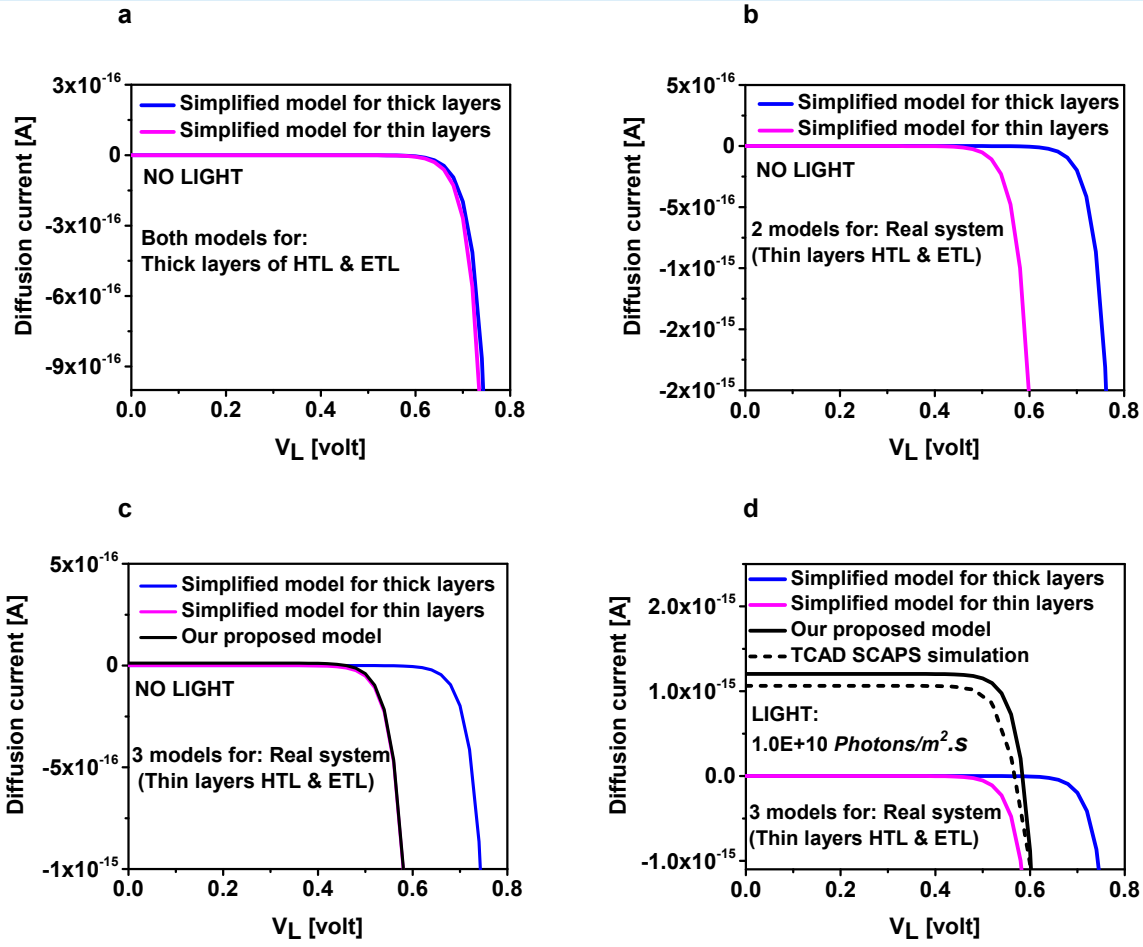

Fig. 3. Comparison of solar cell diffusion current-voltage characteristics predicted by the simplified and and present models. "Thin" and "thick" refer to HTL & ETL with layers thinner and thicker than diffusion length, respectively. (a) A comparison of the diffusion current calculated with the simplified models given by (25) and (29) for a device with thick ETL and HTL, (b) a large mismatch in the open-circuit voltage is predicted by the two simplified models when the transport layer thicknesses are below the minority-carrier diffusion lengths, (c) a comparison of the $\boldsymbol{I-V}$ characteristics obtained from our model with the two simplified models in the dark, for a device with thin transport layers, and (d) a comparison of the $\boldsymbol{I-V}$ characteristics of the tree models under low light illumination for thin transportation layers.

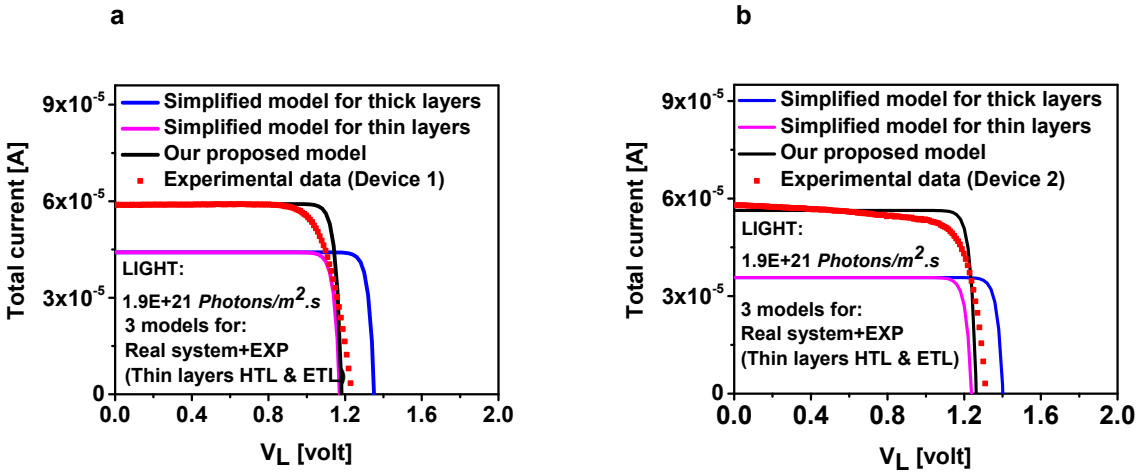

Fig. 4. Total current-voltage characteristics of two wide-bandgap photovoltaic cells, i.e. (a) device 1, (b) device 2, with no difference in fabrication process steps. Comparison of the two simplified and the new models to experimental data and simulation results at room temperature. The scan rate was 20 mV/s.

Fig 3d compares the $I-V$ characteristics of the tree models under low light illumination, i.e. $\phi_0 = 10^{10}$ photons/sec, for thin transportation layers ($T_{\rm e} = T_{\rm h} = 150\,$nm). In this comparison, only the proposed model predicts a finite short-circuit current ($I_{\rm sc}$), which is not properly predicted by the simplified models. $I_{\rm sc}$ cannot be estimated by the drift current (20) only. In the simplified approaches the fail in predicting a finite value of $I_{\rm sc}$ stems from neglecting optical generation in the electron and hole transportation layers when deriving the minority carrier currents. A direct consequence of practical

TABLE IV
EXTRACTED SEMICONDUCTOR PHYSICAL QUANTITIES OF THE FABRICATED CELLS USING OUR PROPOSED MODEL.

Parameter	Device 1	Device 2
Perovskite band-gap, E_g [eV]	2.3	2.3
Absorption coefficient, α [m^{-1}]	8.4×10^{-5}	7.9×10^{-5}
Incident photon flux, ϕ_0 [photon/m^2 s]	1.9×10^{21}	1.9×10^{21}
Thickness of perovskite layer, W_{pr}[nm]	330	330
Thickness of ETL, T_e [nm]	160	160
Thickness of HTL, T_h[nm]	130	130
Doping of HTL, N_A[cm^{-3}]	1.4×10^{17}	1.6×10^{17}
Doping of ETL, N_D[cm^{-3}]	1.3×10^{17}	1.2×10^{17}
E-mobility of ETL, μ_n [cm^2/V Sec]	7.1	3.2
H-mobility of HTL, μ_p [cm^2/V Sec]	4.4	1.2
Electron life time in ETL , τ_n [Sec]	10^{-6}	10^{-6}
Hole life time in HTL , τ_p [Sec]	10^{-6}	10^{-6}
E-diffusion coefficient, D_n [cm^2/Sec]	0.18963	0.08127
H-diffusion coefficient, D_p [cm^2/Sec]	0.1192	0.0325

importance is that these models fail in predicting the maximum power mode of operation, the fill factor, and therefore the efficiency of photovoltaic cell.

Even though the ultimate goal of the model is to quantitatively describe experimental results, an important preliminary step concerns the derivation of a physics-based model. To confirm the validity of the model, its results were compared to simulations obtained using the SCAPS package [22], plotted in Fig 3d. This comparison shows a good agreement between the model and simulated I-V characteristic.

IV. EXPERIMENTS

A. Solar cell device fabrication

1) Substrate and ETL preparation: Fluorine-doped tin oxide (FTO) pre-etched substrates (Sigma-Aldrich, TEC-7) were cleaned by ultrasonication in 2% Hellmanex water solution, isopropyl alcohol (IPA) and ethanol. Next, all the substrates were cleaned by a plasma treatment for 5 min. A compact TiO_2 layer was deposited on FTO by spray pyrolysis, using oxygen as a carrier gas, at 450 °C from a precursor solution of titanium diisopropoxide bis(acetylacetonate) stock solution (75 wt.% in isopropanol) and acetylacetone in anhydrous ethanol. Then, a mesoporous TiO_2 layer was deposited by spin coating using a 30 nm particle paste (Dyesol 30 NR-D) diluted in ethanol (100 $mgmL^{-1}$). After the spin coating, the substrates were sintered with a ramped-up temperature profile. A Li-treatment of mesoporous TiO_2 was performed by spin coating a 10 $mgmL^{-1}$ solution of bis(trifluoromethane)sulfonimide lithium salt (Li-TFSI) in acetonitrile. After cooling down, the substrates were transferred into a nitrogen atmosphere glove box to deposit the perovskite films.

2) Perovskite precursor solution and film preparation: A $MAPbBr_3$ solution was prepared from a precursor solution containing MABr and $PbBr_2$ (1.4 M) in anhydrous DMF:DMSO 3:1 (v:v). $MAPbBr_3$ films were prepared by the flash infrared annealing (FIRA), which include the spin-coating of the perovskite solution in a single step at 4000 rpm for 10 s [23]–[29]. The substrates were then IR irradiated for 1.4 s in the FIRA oven and were kept there for 20 additional seconds before removal and cooling within several min. The FIRA processing was done in a glove box.

3) Hole transport layer and top electrode: After the perovskite annealing, the substrates were cooled down for a few minutes and a spiro-OMeTAD (Lumtec) solution (70 mM in chlorobenzene) was spin coated at 4000 rpm for 20 s. Spiro-OMeTAD was doped with Li-TFSI (SigmaAldrich) and 4-tert-butylpyridine (TBP, SigmaAldrich). Finally, 80 nm of gold was thermally evaporated under high vacuum as top electrode.

B. Experimental results

Two perovskite solar cells were fabricated with the same active area of $16 \times 25\,mm^2$ (Fig. 1c). Cross-sectional scanning electron microscopy (SEM) images of fabricated device is shown in Fig. 1d. The typical thicknesses of the compact and mesoporous TiO_2 layer, the perovskite ($MAPbBr_3$) and spiro-OMeTAD were about 185, 330 and 120 nm, respectively.

The fabricated devices were tested under simulated solar irradiation (100 mW/cm^2, AM 1.5G) using a solar simulator from ABET Technologies (Model Sun 2000) with a xenon arc lamp, and the solar cell response was recorded using a Metrohm PGSTAT302N Autolab. The light intensity was calibrated using a silicon reference cell from ReRa Solutions (KG5 filtered) [23]. Current-voltage curves were measured using a scan rate of 20 mVs^{-1}. The cells were masked with a black metal mask (area: 0.09936 cm^2) in order to fix the active area and reduce the influence of the scattered light.

The current-voltage ($I - V$) curves of a the two devices are shown in Fig. 4. The first cell (Device 1) had a PCE of 5.58%, V_{OC} = 1.24 V, J_{SC} = 5.92 mA cm^{-2} and FF = 76.3%. The second cell (Device 2) achieved a PCE of 5.68%, V_{OC} = 1.31 V, J_{SC} = 5.8 mA cm^{-2} and FF = 74.2%. As demonstrated in Fig. 4, the developed model for PSCs captures precisely the measured current-voltage characteristics of our fabricated devices, while the previously published models fail at predicting those characteristics with the same set of physical parameters.

V. MODEL ASSESSMENT AND PARAMETER EXTRACTION

The model was validated by comparing the simulation results with the experimental data. The output characteristics of the devices and the simulations at room temperature are shown in Fig 4. The agreement between the model and the measurements is good for the whole range of operation. Due to the inclusion of relevant effects and the accuracy over a very broad voltage range, the model is able to predict the behavior of these solar cell and can be used to extract the model parameters in a fast and reliable manner.

The parameter extraction starts by extracting the absorption coefficient α, followed by the extraction of the other parameters, such as doping concentrations, mobility and lifetime of carriers in the transport layers from the plots. Table IV gives the values of the relevant parameters used in the model. Therefore, relying on the new model, the parameters identification for photovoltaic cells and also technological parameters are accurately extracted from our experimental results unlike with using simplified approaches.

VI. Conclusion

Up to now, the impact of optical generation in the quasi-neutral regions has been neglected in analytical models of PSCs. This assumption, which is still widely accepted and implemented, fails in predicting accurately the influence of the various parameters of the photovoltaic cells on the output characteristics. This article adopts a drift-diffusion transport mechanism that includes the local optical generation across the entire device structure and develops a physics-based model of perovskite photovoltaic cells that can predict the device characteristics from the device parameters, significantly improving earlier approaches. This modeling approach was verified by measurements of fabricated perovskite cells. Our new model will allow the optimization of perovskite solar cells, making use of a simple set of analytical relationships.

Acknowledgment

E.O.M. acknowledges funding by a Swiss Government Excellence Scholarship (2017.1080) and by a European Union's Horizon 2020 Research and Innovation Programme under the Marie Sklodowska-Curie project PerSisTanCe with grant agreement No. 841005. J.V.M. is grateful for the Swiss National Foundation PRIMA grant no. 19374. This works was partially funded by the Adolphe Merkle Foundation (P.F., U.S. and J.V.M).

References

[1] M. Saliba, T. Matsui, J.-Y. Seo, K. Domanski, J.-P. Correa-Baena, M. K. Nazeeruddin, S. M. Zakeeruddin, W. Tress, A. Abate, A. Hagfeldt, and M. Grätzel, "Cesium-containing triple cation perovskite solar cells: improved stability, reproducibility and high efficiency," *Energy Environ. Sci.*, vol. 9, pp. 1989–1997, March 2016. [Online]. Available: http://dx.doi.org/10.1039/C5EE03874J

[2] M. Saliba, T. Matsui, K. Domanski, J.-Y. Seo, A. Ummadisingu, S. M. Zakeeruddin, J.-P. Correa-Baena, W. R. Tress, A. Abate, A. Hagfeldt, and M. Grätzel, "Incorporation of rubidium cations into perovskite solar cells improves photovoltaic performance," *Science*, vol. 354, no. 6309, pp. 206–209, October 2016. [Online]. Available: 10.1126/science.aah5557

[3] A. Kojima, K. Teshima, Y. Shirai, and T. Miyasaka, "Organometal halide perovskites as visible-light sensitizers for photovoltaic cells," *Journal of the American Chemical Society*, vol. 131, no. 17, pp. 6050–6051, April 2009. [Online]. Available: https://doi.org/10.1021/ja809598r

[4] "Best res.-cell efficiency," https://www.nrel.gov/pv/cell-efficiency.html, March 2020.

[5] S. P. Malyukov, A. V. Sayenko, and A. V. Ivanova, "Numerical modeling of perovskite solar cells with a planar structure," *IOP Conference Series: Materials Science and Engineering*, vol. 151, no. 17, p. 012033, October 2016. [Online]. Available: https://doi.org/10.1088/1757-899x/151/1/012033

[6] X. Sun, R. Asadpour, W. Nie, A. D. Mohite, and M. A. Alam, "A physics-based analytical model for perovskite solar cells," *IEEE Journal of Photovoltaics*, vol. 5, no. 5, pp. 1389–1394, September 2015. [Online]. Available: https://doi.org/10.1109/JPHOTOV.2015.2451000

[7] A. Rolland, L. Pedesseau, Y. Huang, S. Wang, D. Sapori, C. Cornet, O. Durand, J. Even, M. Kepenekian, and C. Katan, "Computational design of high performance hybrid perovskite on silicon 2-T tandem solar cells based on a tunnel junction," in *2017 International Conference on Numerical Simulation of Optoelectronic Devices (NUSOD)*, July 2017, pp. 67–68. [Online]. Available: https://doi.org/10.1109/NUSOD.2017.8009994

[8] Y. Raoui, H. Ez-Zahraouy, N. Tahiri, O. El Bounagui, S. Ahmad, and S. Kazim, "Performance analysis of $MAPbI_3$ based perovskite solar cells employing diverse charge selective contacts: Simulation study," *Solar Energy*, vol. 193, pp. 948 – 955, November 2019. [Online]. Available: https://doi.org/10.1016/j.solener.2019.10.009

[9] P. Basore, "Numerical modeling of textured silicon solar cells using PC-1D," *IEEE Transactions on Electron Devices*, vol. 37, no. 2, pp. 337–343, February 1990. [Online]. Available: https://doi.org/10.1109/16.46362

[10] G. A. Vokas, A. V. Machias, and J. L. Souflis, "Computer modeling and parameters estimation for solar cells," in *[1991 Proceedings] 6th Mediterranean Electrotechnical Conference*, vol. 1, May 1991, pp. 206–209. [Online]. Available: https://doi.org/10.1109/MELCON.1991.161813

[11] J. G. Fossum, "Computer-aided numerical analysis of silicon solar cells," *Solid-State Electronics*, vol. 19, no. 4, pp. 269 – 277, April 1976. [Online]. Available: https://doi.org/10.1016/0038-1101(76)90022-8

[12] T. Minemoto and M. Murata, "Device modeling of perovskite solar cells based on structural similarity with thin film inorganic semiconductor solar cells," *Journal of Applied Physics*, vol. 116, no. 5, p. 054505, August 2014. [Online]. Available: https://doi.org/10.1063/1.4891982

[13] W. Xiao, W. G. Dunford, and A. Capel, "A novel modeling method for photovoltaic cells," in *2004 IEEE 35th Annual Power Electronics Specialists Conference (IEEE Cat. No.04CH37551)*, vol. 3, June 2004, pp. 1950–1956. [Online]. Available: https://doi.org/10.1109/PESC.2004.1355416

[14] Y. Huang, "Modeling of Perovskite Solar Cells, III-V Optoelectronic Devices and Kelvin Probe Microscopy," Theses, INSA de Rennes, March 2018. [Online]. Available: https://tel.archives-ouvertes.fr/tel-01881871

[15] N. Tessler and Y. Vaynzof, "Insights from device modeling of perovskite solar cells," *ACS Energy Letters*, vol. 5, no. 4, pp. 1260–1270, March 2020. [Online]. Available: https://doi.org/10.1021/acsenergylett.0c00172

[16] S. Sze and K. K. Ng, *p-n Junctions*. John Wiley & Sons, Ltd, 2006. [Online]. Available: https://onlinelibrary.wiley.com/doi/abs/10.1002/9780470068328.ch2

[17] R. V. K. Chavali, S. De Wolf, and M. A. Alam, "Device physics underlying silicon heterojunction and passivating-contact solar cells: A topical review," *Progress in Photovoltaics: Research and Applications*, vol. 26, no. 4, pp. 241–260, 2018. [Online]. Available: https://onlinelibrary.wiley.com/doi/abs/10.1002/pip.2959

[18] J. E. Moore, S. Dongaonkar, R. V. K. Chavali, M. A. Alam, and M. S. Lundstrom, "Correlation of built-in potential and ¡italic¿i–v¡/italic¿ crossover in thin-film solar cells," *IEEE Journal of Photovoltaics*, vol. 4, no. 4, pp. 1138–1148, 2014.

[19] H. Xi, S. Tang, X. Ma, J. Chang, D. Chen, Z. Lin, P. Zhong, H. Wang, and C. Zhang, "Performance enhancement of planar heterojunction perovskite solar cells through tuning the doping properties of hole-transporting materials," *ACS Omega*, vol. 2, no. 1, pp. 326–336, January 2017. [Online]. Available: https://doi.org/10.1021/acsomega.6b00465

[20] Q. Chen, N. De Marco, Y. M. Yang, T.-B. Song, C.-C. Chen, H. Zhao, Z. Hong, H. Zhou, and Y. Yang, "Under the spotlight: The organic–inorganic hybrid halide perovskite for optoelectronic applications," *Nano Today*, vol. 10, no. 3, pp. 355 – 396, June 2015. [Online]. Available: https://doi.org/10.1016/j.nantod.2015.04.009

[21] S. Almosni, L. Cojocaru, D. Li, S. Uchida, T. Kubo, and H. Segawa, "Tunneling-assisted trapping as one of the possible mechanisms for the origin of hysteresis in perovskite solar cells," *Energy Technology*, vol. 5, no. 10, pp. 1767–1774, July 2017. [Online]. Available: https://onlinelibrary.wiley.com/doi/abs/10.1002/ente.201700246

[22] "Simulation programme scaps-1d for thin film solar cells developed at elis, university of gent," https://scaps.elis.ugent.be/SCAPSinstallatie.html, August 2021.

[23] S. Sánchez, J. Jerónimo-Rendon, M. Saliba, and A. Hagfeldt, "Highly efficient and rapid manufactured perovskite solar cells via flash infrared annealing," *Materials Today*, vol. 35, pp. 9 – 15, May 2020. [Online]. Available: https://doi.org/10.1016/j.mattod.2019.11.003

[24] J. Troughton, C. Charbonneau, M. J. Carnie, M. L. Davies, D. A. Worsley, and T. M. Watson, "Rapid processing of perovskite solar cells in under 2.5 seconds," *J. Mater. Chem. A*, vol. 3, pp. 9123–9127, March 2015. [Online]. Available: http://dx.doi.org/10.1039/C5TA00568J

[25] J. Baker, K. Hooper, S. Meroni, A. Pockett, J. McGettrick, Z. Wei, R. Escalante, G. Oskam, M. Carnie, and T. Watson, "High throughput fabrication of mesoporous carbon perovskite solar cells," *J. Mater. Chem. A*, vol. 5, pp. 18 643–18 650, August 2017. [Online]. Available: http://dx.doi.org/10.1039/C7TA05674E

[26] B. Martin, M. Yang, R. C. Bramante, E. Amerling, G. Gupta, M. F. A. M. van Hest, and T. Druffel, "Fabrication of flexible perovskite solar cells via rapid thermal annealing," *Materials Letters C*, vol. 276, October 2020. [Online]. Available: https://doi.org/10.1016/j.matlet.2020.128215

[27] S. Sánchez, M. Vallés-Pelarda, J.-A. Alberola-Borràs, R. Vidal, J. J. Jerónimo-Rendón, M. Saliba, P. P. Boix, and I. Mora-Seró,

"Flash infrared annealing as a cost-effective and low environmental impact processing method for planar perovskite solar cells," *Materials Today*, vol. 31, pp. 39 – 46, December 2019. [Online]. Available: https://doi.org/10.1016/j.mattod.2019.04.021

[28] S. Sanchez, X. Hua, N. Phung, U. Steiner, and A. Abate, "Flash infrared annealing for antisolvent-free highly efficient perovskite solar cells," *Advanced Energy Materials*, vol. 8, no. 12, p. 1702915, January 2018. [Online]. Available: https://doi.org/10.1002/aenm.201702915

[29] P. Ferdowsi, E. Ochoa-Martinez, S. Sanchez Alonso, U. Steiner, and M. Saliba, "Ultrathin polymeric films for interfacial passivation in wide band-gap perovskite solar cells," *Scientific Reports*, vol. 10, no. 22260, p. 22260, December 2020. [Online]. Available: https://doi.org/10.1038/s41598-020-79348-1